

Article

Design of 2.5D Miniaturized Broadband Absorber for Ultrahigh-Frequency Band

Peipei Wang, Wu Ren ^{*}, Zhenghui Xue and Weiming Li

School of Integrated Circuits and Electronics, Beijing Institute of Technology, Beijing 100081, China; ppei_wang@163.com (P.W.); zhxue@bit.edu.cn (Z.X.); wml@bit.edu.cn (W.L.)

* Correspondence: renwu@bit.edu.cn

Abstract: A broadband metamaterial absorber (MA) structure for Ultrahigh-Frequency (UHF) band was proposed, and the miniaturization of the unit was realized by combining the method of bending metal wires and loading metal vias. The size of the unit cell is $0.040 \lambda_L \times 0.040 \lambda_L \times 0.075 \lambda_L$ (λ_L is the wavelength corresponding to the lowest frequency of 0.5 GHz). The simulation results show that the bandwidth of the MA is from 0.50 GHz to 1.33 GHz, and the relative bandwidth is 90.7%. Polarization insensitivity of the MA was realized through assembling a 2×2 orthogonal array. TE and TM polarizations maintain more than 80% of the absorptance in the range of 40° at oblique incidence. The consistency of full-wave simulation, circuit simulation and measured results is high, which verifies the broadband absorption characteristics of the proposed MA.

Keywords: absorber; 2.5D; wire bending; double-layer; UHF band



Citation: Wang, P.; Ren, W.; Xue, Z.; Li, W. Design of 2.5D Miniaturized Broadband Absorber for Ultrahigh-Frequency Band. *Electronics* **2022**, *11*, 1664. <https://doi.org/10.3390/electronics11101664>

Academic Editor: Giovanni Andrea Casula

Received: 24 April 2022

Accepted: 20 May 2022

Published: 23 May 2022

Publisher's Note: MDPI stays neutral with regard to jurisdictional claims in published maps and institutional affiliations.



Copyright: © 2022 by the authors. Licensee MDPI, Basel, Switzerland. This article is an open access article distributed under the terms and conditions of the Creative Commons Attribution (CC BY) license (<https://creativecommons.org/licenses/by/4.0/>).

1. Introduction

Since Landy successfully designed the first MA [1], rich research results of MAs have been accumulated in terms of structural forms and design principles. However, current researches on stealth materials mainly focus on X and Ku bands [2–4], while researches on UHF band are less. It is because the attenuation constant of the material decreases significantly at low frequency, and the electrical size corresponding to the low frequency is relatively large, which is difficult to meet the need for miniaturization in practical applications.

Combined with current research, the low-frequency technology of MAs can be divided into two categories. One is to lower the position of the resonance point by lumped elements, and the other is to use the convolution geometry method to increase the length of metal wire by bending, winding, etc. In 2017, Xuan K B et al. proposed a design method of absorbers loaded by capacitors [5]. Four lumped capacitors embedded between metal patches effectively lower the resonant frequency. Experimental results show that the structure achieves perfect absorption at 102 MHz, and the unit size is reduced to $35 \times 35 \text{ mm}^2$. Then, in order to verify the contribution of capacitors to the resonant frequency regulation, two capacitors with different capacitance values were loaded into the unit [6] so that the MA realized double absorption peaks at 304.9 MHz and 358.5 MHz. Inductors were also applied in low-frequency technology research of MAs. Jeong H et al. [7] connected the metal square ring with four inductors and indicated that the absorption frequency was inversely proportional to the inductance value of the inductors. In addition, Buitung S innovatively proposed an hourglass-type absorber structure on the basis of curved lines [8], which can obtain a narrow-band absorption peak near 377 MHz. Araneo R et al. designed a complex helical unit structure by using tightly arranged helical lines to enhance the coupling effect in MA [9] and achieved perfect absorption at 395 MHz. Although the above designs achieve low-frequency absorption, it is a common problem that the bandwidths of designed MAs are not wide enough. In 2016, a compact MA for the UHF band was designed in [10], and it

bends the square metal ring loaded with resistors inward several times. Without affecting the frequency response, it reduces the unit size to a quarter of the metal square ring, but the absolute bandwidth of the MA is only 150 MHz. In order to improve the bandwidth, the bending method of metal wires, the number of lumped resistors and the thickness of the air layer were further optimized in [11], thereby introducing more resonance points in MA. The research successfully realizes a low-frequency broadband MA operating from 0.8 GHz to 2.7 GHz.

The above research results enrich the design ideas of low-frequency MAs, but they are all optimized based on traditional 2D structures. In recent years, 3D structures [12,13] and 2.5D structures [14–17] have been widely used in the design of metamaterials. Unlike 3D structures, 2.5D structures show wide-band and low-frequency characteristics without changing the profile height. Typical structures of 2.5D are proposed in [14,15]. Metal vias can increase the capacitance and inductance in the equivalent circuit. In addition, it can connect a longer circuit in MA, which is conducive to the realization of low-frequency. With a systematic study of the equivalent circuit with metal vias [16], Yi-min et al. introduced vertical vias into the design of frequency selective surface and proposed the calculation formula of equivalent capacitance and equivalent inductance. In addition, the research verifies the great potential of metal vias in low-frequency characteristics through simulation and measurement. On this basis, 36 metal vias were introduced in MA, further reducing the resonant frequency to 1890 MHz [17].

In this paper, a MA structure for the UHF band based on 2.5D is proposed, which can achieve more than 90% absorptance in the range from 500 MHz to 1330 MHz. We established a simplified equivalent circuit model and verified the simulation results experimentally. According to simulation and measurement results, the proposed MA achieves the comprehensive performance of wide-band, miniaturization, low frequency and low profile. On the one hand, it can effectively reduce electromagnetic interference and improve the complex electromagnetic environment. Thus, it can improve stability when applied to UHF-RFID systems. In addition, the proposed MA can also be applied to the field of stealth in the UHF band, absorbing electromagnetic waves reflected in the environment to achieve perfect stealth.

2. Unit Cell Design and Simulation

By combining the methods of bending lines and metal vias, a 2.5D double-layer MA unit was proposed. As shown in Figure 1a, layers composing the unit structure from top to bottom are Metal-Layer I, Dielectric-Layer I, Metal-Layer II, Dielectric-Layer II, Metal-Layer III, Air-Layer and Reflection-Layer. Figure 1b,c show the structures of the three Metal-Layers. The structures of Metal-Layer I and Metal-Layer III are completely the same, and they are orthogonal to Metal-Layer II in the middle. The purple and green patches in Figure 1b are resistors with values $R_a = 91 \Omega$ and $R_b = 100 \Omega$. It can be seen that resistors are only designed on the Metal-Layer I and the Metal-Layer III. This is because the Metal-Layer II is located between the double Dielectric-Layers, and it is not suitable to load lumped elements with thickness during the fabrication. Metal-Layers are arranged on the upper and lower surfaces of the Dielectric-Layers and connected by multiple metal vias to form a closed loop in Figure 1d. Unlike 3D structures, the introduction of vias does not increase the profile height of the MA, so it is called a 2.5D structure. Metal holes passing through the Dielectric-Layers connect the upper and lower circuits, and it means that metal patches can be designed as longer loops in the same unit, increasing the level of miniaturization of MA.

Figure 1e shows the multi-layer structure of the MA unit cell. In order to achieve better low-frequency characteristics, the MA is laminated with double FR4 ($\epsilon_{r1} = 4.4$, $\tan\delta = 0.2$) Dielectric-Layers, and the thickness of the single Dielectric-Layer is $h_1/2 = 2.4$ mm. The Air-Layer ($\epsilon_{r0} = 1.0$) with a thickness of $h_0 = 40$ mm is located between the Dielectric-Layer and the Reflection-Layer, which is conducive to the realization of broadband matching with free space. Due to the symmetry of the MA, we only marked geometry dimensions

of one-eighth of the bend line on the top view of Figure 1f. Simulation settings of the MA in HFSS are shown in Figure 1a. The MA is excited by a floquet port, and the sides of the unit are set to the master and slave boundary. The geometric parameters in MA were adjusted to achieve the best broadband characteristics, and the final geometric dimensions are optimized as: $a_1 = 8.4$ mm, $a_2 = 5.6$ mm, $a_3 = 2.4$ mm, $a_4 = 6.6$ mm, $b_1 = 2.4$ mm, $b_2 = 5.6$ mm and $b_3 = 4$ mm. In addition, the period of the MA is $p = 23.8$ mm, and the width of the wire is $w = 0.5$ mm.

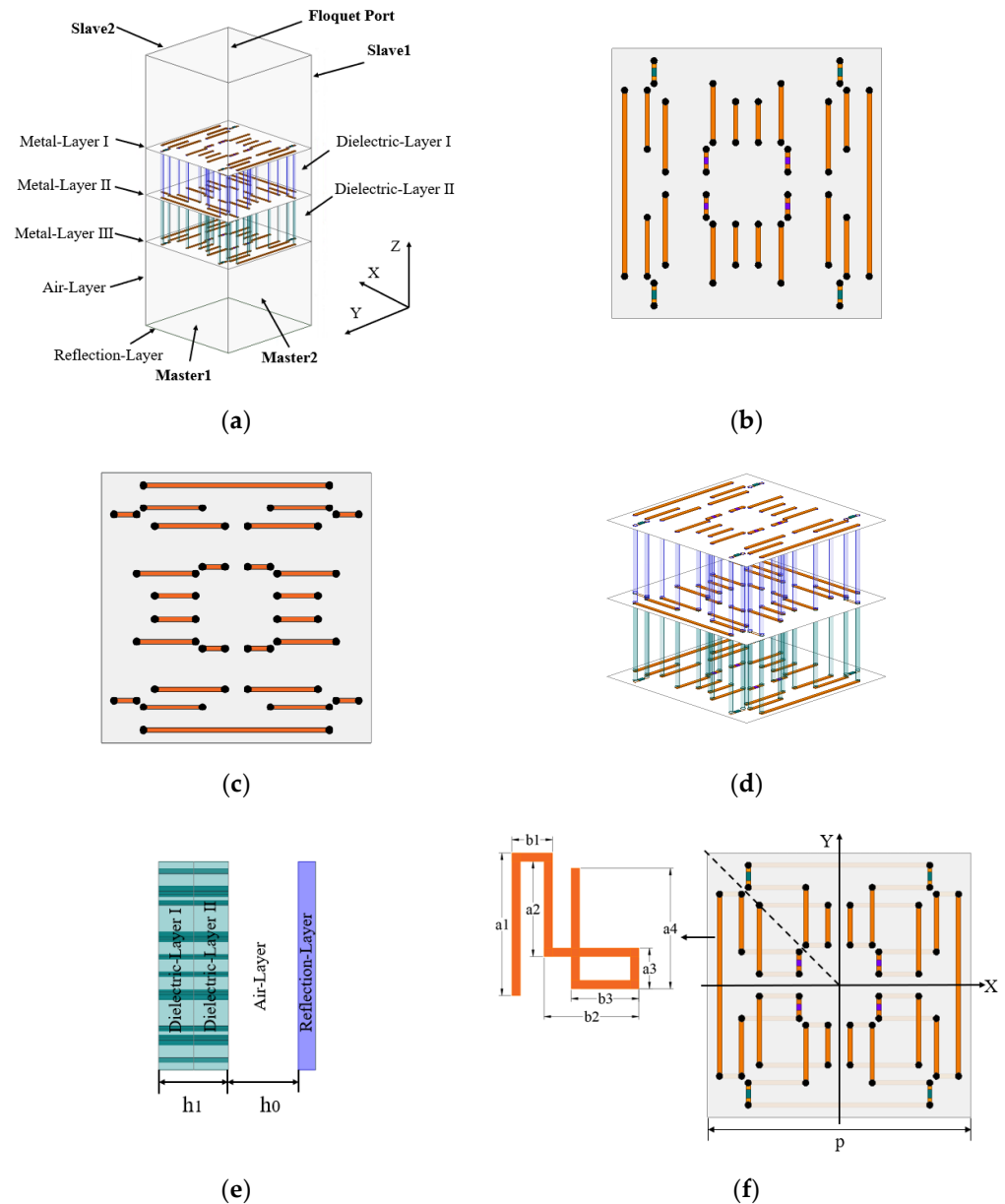


Figure 1. Geometry of 2.5D absorber unit cell: (a) multi-layer structure, (b) Metal-Layer I and Metal-Layer III, (c) Metal-Layer II, (d) perspective view, (e) side view and (f) top view.

Simulation results of the MA are shown in Figure 2. Due to the existence of the Reflection-Layer, the absorptance can be calculated by $A(\omega) = 1 - R(\omega) = 1 - |S_{11}|^2$. It can be seen that the bandwidth of TE mode is 0.47 GHz to 1.00 GHz, and that of TM mode is 0.47 GHz to 1.06 GHz. The absorption peaks are formed around 550 MHz and 880 MHz in both modes, but trends of reflection coefficient curves are quite different. It is because three Metal-Layers are not completely identical. Generally speaking, such MAs without quadruple rotational symmetry are polarization-sensitive.

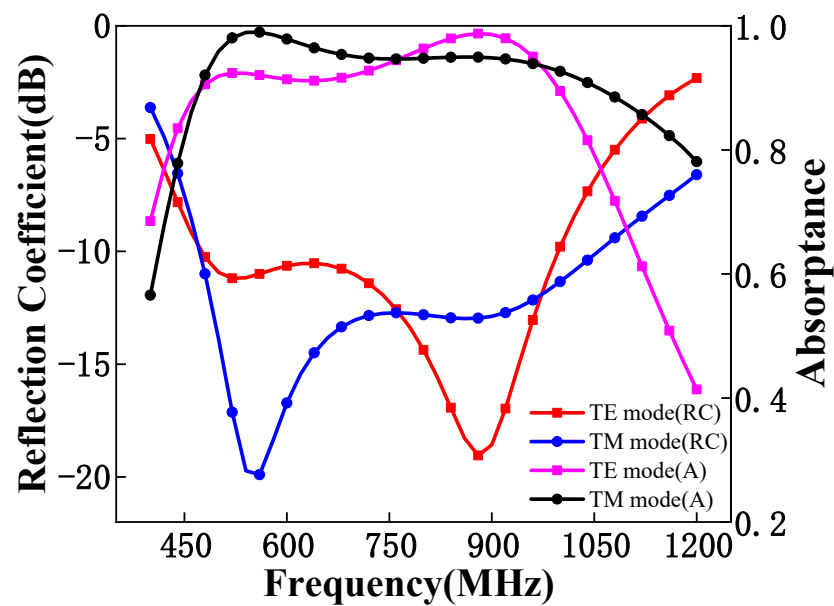


Figure 2. The reflection coefficient and absorptance of MA in TE and TM modes.

Next, we further eliminated the polarization sensitivity of the MA by forming arrays. As shown in Figure 3, we rotated the MA1 along the Z-axis to obtain the orthogonal unit MA2 and stagger them on a 2×2 array. MA1 and MA2 have negligible phase differences to plane incident waves under infinite-period boundary conditions. Therefore, the arrayed MAs can produce nearly equal absorption for TE and TM modes when the array scale is large enough.

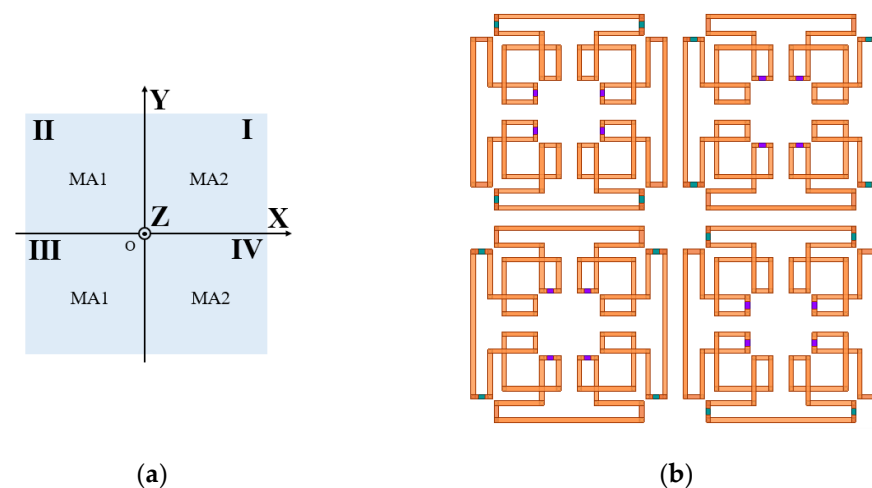


Figure 3. Schematic diagram of the arrayed MAs: (a) array distribution and (b) top view.

From the simulation results in Figure 4, the bandwidth of the proposed structure meeting the requirements of the absorptance above 90% is 500 MHz to 1330 MHz, and the relative bandwidth is 90.7%. The MA unit cell is miniaturized through wire bending. The unit cell size is $23.8 \text{ mm} \times 23.8 \text{ mm}$, and the profile height is 44.8 mm. Two absorption peaks of the arrayed MA are formed at $F_L = 0.59 \text{ GHz}$ and $F_H = 1.13 \text{ GHz}$ with reflection coefficients of -19.6 dB and -22.7 dB and absorptance of 98.9% and 99.5%. It is due to the blocking effect of resistors with different resistance values, which cuts the closed-loop into current paths of different lengths, which can further adjust the position of F_L and F_H to realize broadband absorption at low frequency. It can be seen that the curves at different polarizations basically coincide, and the arrayed MAs achieve polarization insensitivity.

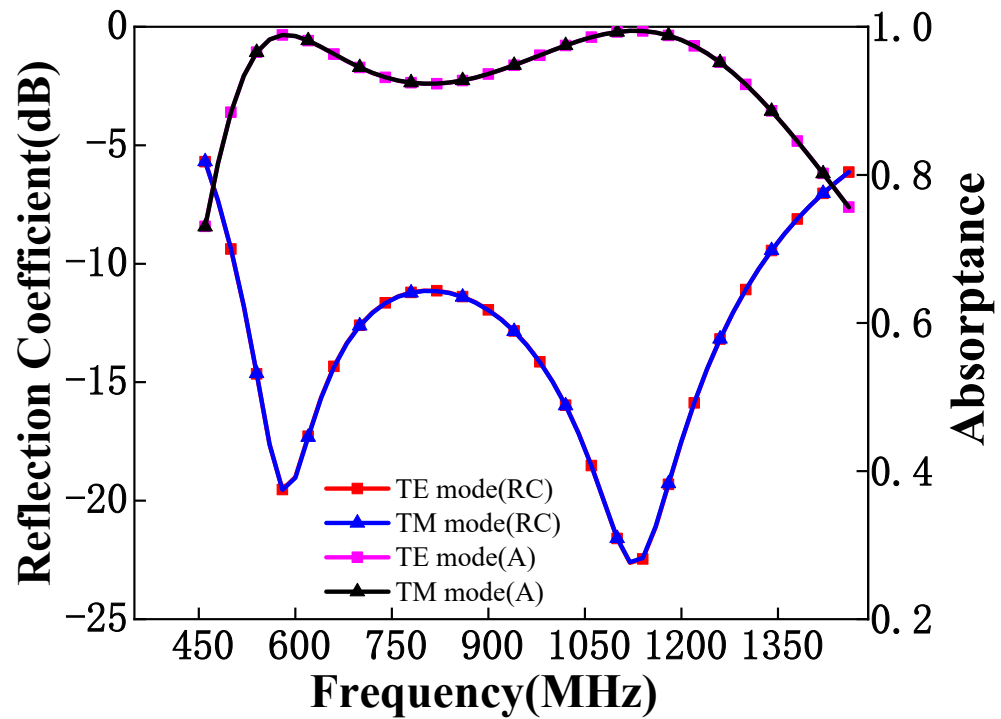


Figure 4. The reflection coefficient and absorbance of the arrayed MAs in TE and TM modes.

Figure 5 shows the simulated absorbance curves of TE and TM polarizations at different oblique incident angles. As shown in Figure 5a, with the increase in oblique incident angle, the position of F_L in TE polarization basically does not change, while F_H gradually moves slightly to a high frequency. In addition, the absorbance gradually decreased within the bandwidth, and the depression between F_L and F_H gradually deepened. Different from TE polarization, the absorption curve of TM polarization has a more obvious blue shift under oblique incidence, and the low-frequency characteristics are gradually lost. In general, the 2.5D structure maintains more than 80% of the absorbance under the incident angle of 40° and has good oblique incidence stability.

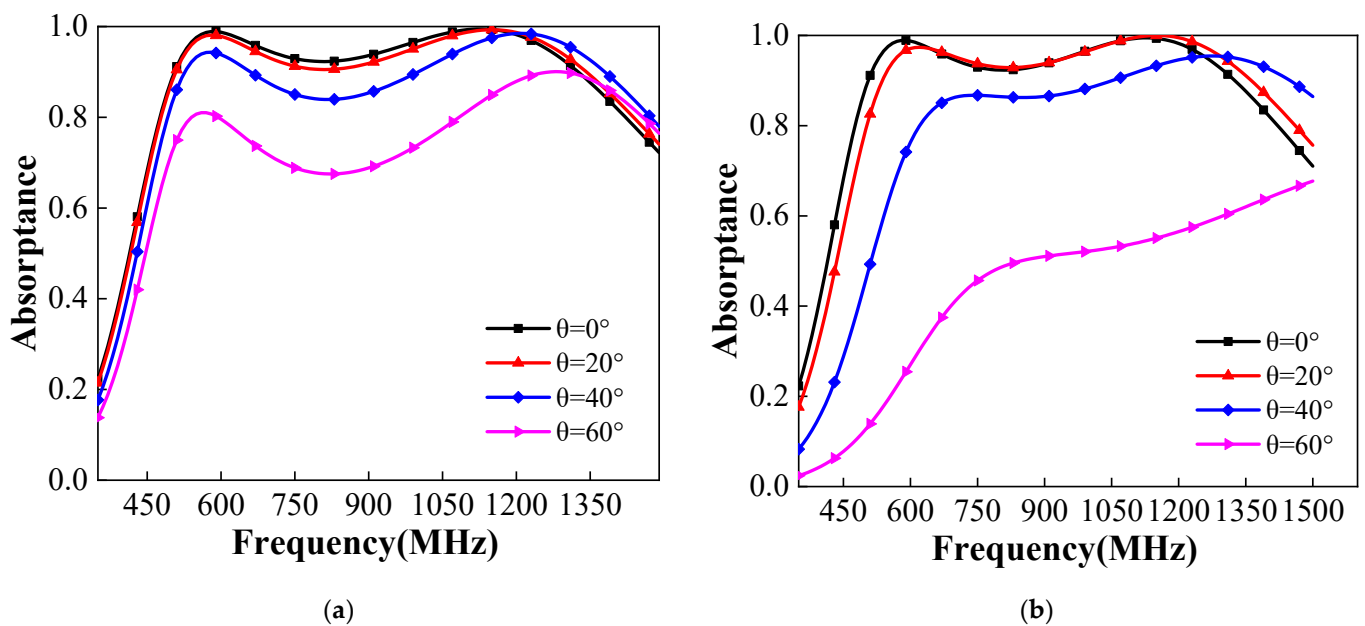


Figure 5. Reflection coefficient for oblique incident: (a) TE mode and (b) TM mode.

3. Absorption Mechanism

We proposed a simplified equivalent circuit model based on transmission-line theory. As shown in Figure 6, the bent metal wire is composed of two parallel resonant loops in series. The Dielectric-Layer and Air-Layer are equivalent to uniform transmission lines, and the Reflection-Layer is represented by a short-circuit line.

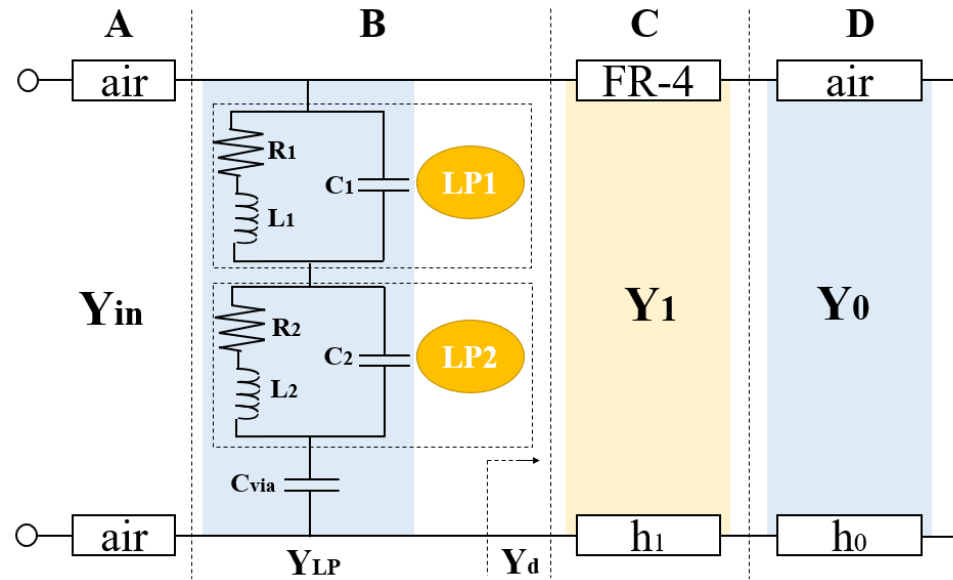


Figure 6. Simplified equivalent circuit model based on transmission-line theory.

Section A in Figure 6 represents the transmission line in free space, which characteristic impedance is $Z_0 = 377 \Omega$, and the electromagnetic wave of normal incidence enters the surface of the MA through A. Section B is the Metal-Layers in MA. LP1 and LP2 loops generate low and high-frequency resonance points, respectively, whose admittances are represented by Y_{LP1} and Y_{LP2} . The coupling effect of metalized vias between adjacent units is represented by the supplementary capacitance C_{via} . Sections C and D are equivalently modeling the Dielectric-Layer and Air-Layer. Sections C simulates a transmission line with characteristic impedance Z_1 and length h_1 . Sections D simulates a transmission line with characteristic impedance Z_0 and length h_0 .

The admittances of LP1, LP2 loops and C_{via} are expressed as follows.

$$Y_{LP1} = \frac{1}{R_1 + j\omega L_1} + j\omega C_1 \tag{1}$$

$$Y_{LP2} = \frac{1}{R_2 + j\omega L_2} + j\omega C_2 \tag{2}$$

$$Y_{via} = j\omega C_{via} \tag{3}$$

so

$$Y_{LP} = \frac{1}{\frac{1}{Y_{LP1}} + \frac{1}{Y_{LP2}} + \frac{1}{Y_{via}}} = G_{LP} + jB_{LP} \tag{4}$$

According to transmission-line theory, Y_d is expressed as

$$Y_d = Y_1 \cdot \frac{(-jY_0 \cdot \cot(\beta_0 \cdot h_0)) + jY_1 \cdot \tan(\beta_1 \cdot h_1)}{Y_1 + j(-jY_0 \cdot \cot(\beta_0 \cdot h_0)) \cdot \tan(\beta_1 \cdot h_1)} \tag{5}$$

$$= j \frac{Y_1(Y_1 \cdot \tan(\beta_1 \cdot h_1) - Y_0 \cdot \cot(\beta_0 \cdot h_0))}{Y_1 + Y_0 \cdot \cot(\beta_0 \cdot h_0) \cdot \tan(\beta_1 \cdot h_1)} = jB_d$$

Y_0 and Y_1 are the admittance forms corresponding to the characteristic impedances Z_0 and Z_1 . The admittance corresponding to the input impedance Z_{in} of the MA can be expressed as.

$$Y_{in} = \frac{1}{Z_{in}} = \frac{1}{Z_d} + \frac{1}{Z_{LP}} = Y_d + Y_{LP} = G_{LP} + j(B_d + B_{LP}) \tag{6}$$

where, $Y_i = Y_0 \cdot \sqrt{\epsilon_{ri}}$, $\beta_i = 2\pi\sqrt{\epsilon_{ri}}/\lambda$, $i = 0, 1$, $w = 2\pi f$, $Y_0 = 1/Z_0 = 1/377S$. According to the transmission-line theory mentioned above, the reflection coefficients of the model at discrete points are calculated in ADS, and the simulation results of each discrete point are fitted into a smooth reflection coefficient curve. Then, the parameter values of the lumped elements in the circuit model are optimized to achieve the minimum error between the circuit and the full-wave simulations. The circuit component values in the model are optimized as follows: $R_1 = 85 \Omega$, $C_1 = 0.85 \text{ pF}$, $L_1 = 18 \text{ nH}$, $R_2 = 60 \Omega$, $C_1 = 0.20 \text{ pF}$, $L_1 = 3.6 \text{ nH}$ and $C_{via} = 1.20 \text{ pF}$. To verify the accuracy of the model, we compare the results of ADS circuit simulation and HFSS full-wave simulation in Figure 7. The results show that the variation trend of the absorption curve in bandwidth is consistent with the full-wave simulation. The working bandwidth of the circuit simulation is 515 MHz to 1310 MHz, and the positions of the two absorption peaks basically coincide.

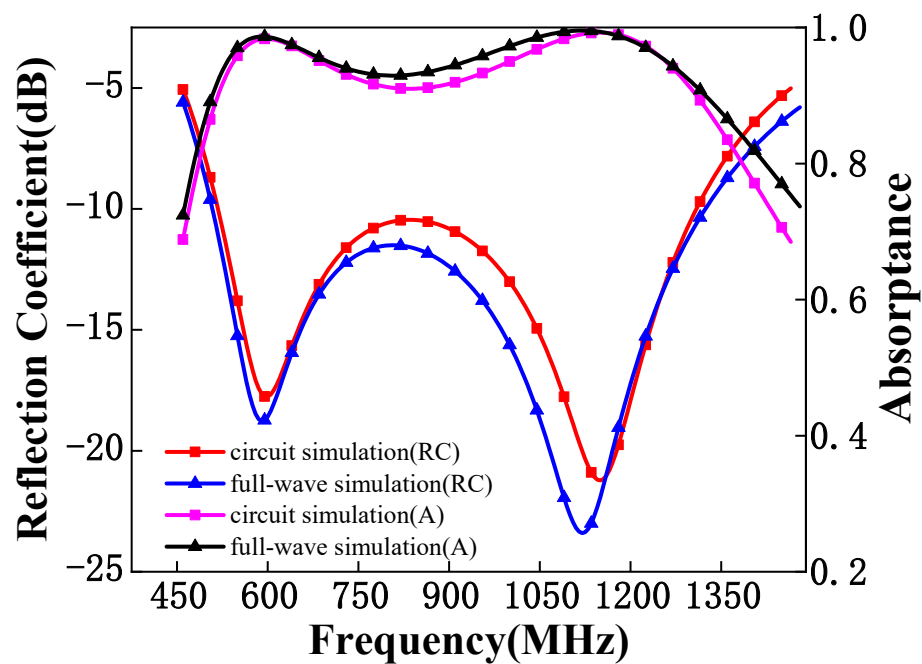


Figure 7. Comparison of reflection coefficients between circuit simulation and full-wave simulation.

In order to further understand the generation mechanism of the double resonance point, we studied the real and imaginary parts of Y_{in} in the equivalent circuit. According to Equations (4) to (6), we plotted the curves of G_{LP} , B_d , B_{LP} and B_d plus B_{LP} in Figure 8. It can be seen in Figure 8a that the sum of B_d and B_{LP} is 0 at $f_1 = 600 \text{ MHz}$, $f_2 = 762 \text{ MHz}$ and $f_3 = 1089 \text{ MHz}$, which means that the imaginary part of Y_{in} is 0. In general, the real part of the impedance that can generate resonance should match Z_0 , and the conductance range corresponding to $(377 \pm 50) \Omega$ is marked in the gray part shown in Figure 8b. The conductance of f_1 and f_3 are within the matching range of the free space, which is basically consistent with F_L and F_H in full-wave simulation. However, the G_{LP} at f_2 is about 0.005, corresponding to a characteristic impedance of about 200Ω . It is quite different from the characteristic impedance of free space, resulting in a mismatch, so there is no absorption peak at f_2 .

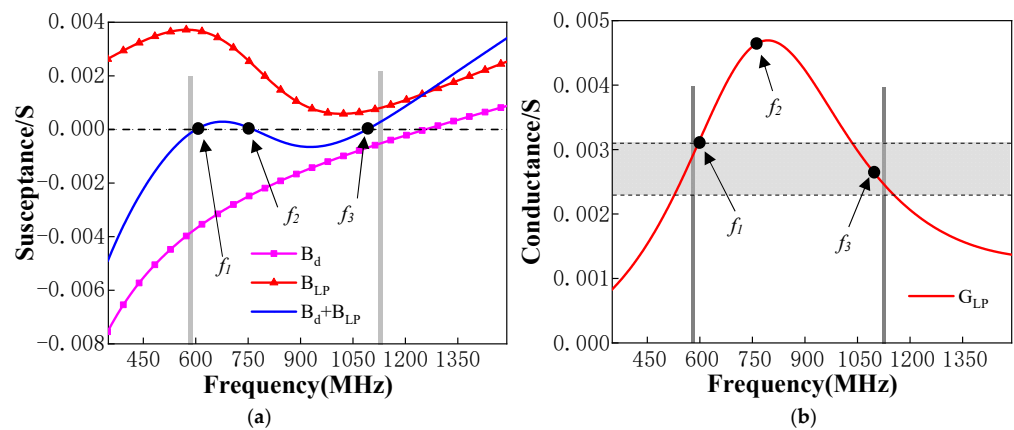


Figure 8. Input admittance obtained from the equivalent circuit: (a) imaginary parts of Y_d , Y_{LP} and Y_{in} , and (b) real part of Y_{LP} .

4. Experiment Results and Discussions

As shown in Figure 9a,b, the MA is fabricated with a dimension of 400 mm \times 400 mm (16 cells \times 16 cells), and Teflon nuts and bolts are used to control the thickness of the air gap. The measurement system of the fabricated absorber is shown in Figure 9d, and the reflection coefficient of the sample in free space was measured with a log-periodic antenna operating from 0.4 GHz to 3 GHz.

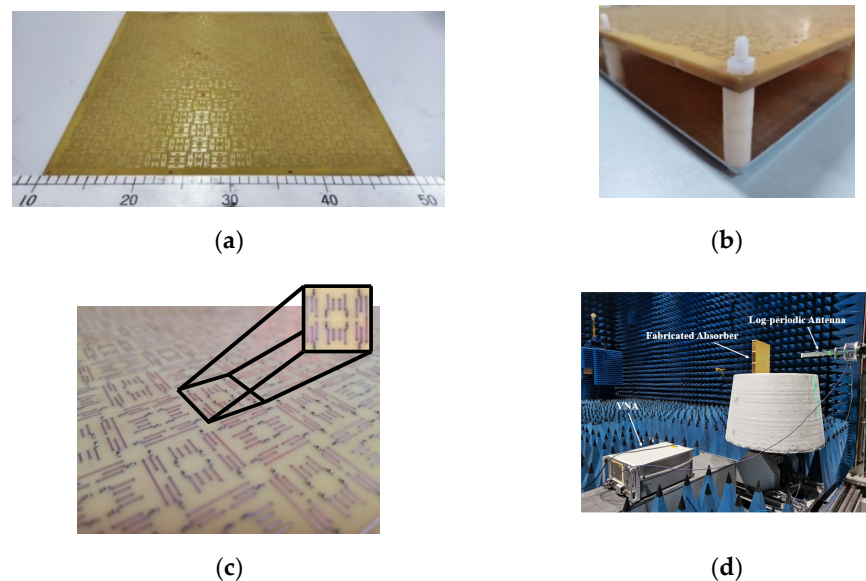


Figure 9. Fabricated absorber and measurement environment: (a) top view of the prototype, (b) side view of the prototype, (c) complete view of the prototype and (d) experimental setup in the anechoic chamber.

Calibrate the environment with a metal aluminum plate of the same scale, and the difference between it and the fabricated MA is the true reflection coefficient of the sample. As shown in Figure 10, the measured reflection coefficient less than -10 dB under normal incidence is from 535 MHz to 1310 MHz. Compared with simulation results, it can be seen that the bandwidth and the position of the F_L and F_H in experimental results are basically accurate. However, the absorptance of the experiment results is generally lower. It is because the copper adsorbed on the surface of the through-hole during fabrication is not uniform enough, which leads to the poor conduction effect of some circuits, thus causing errors during the experiment.

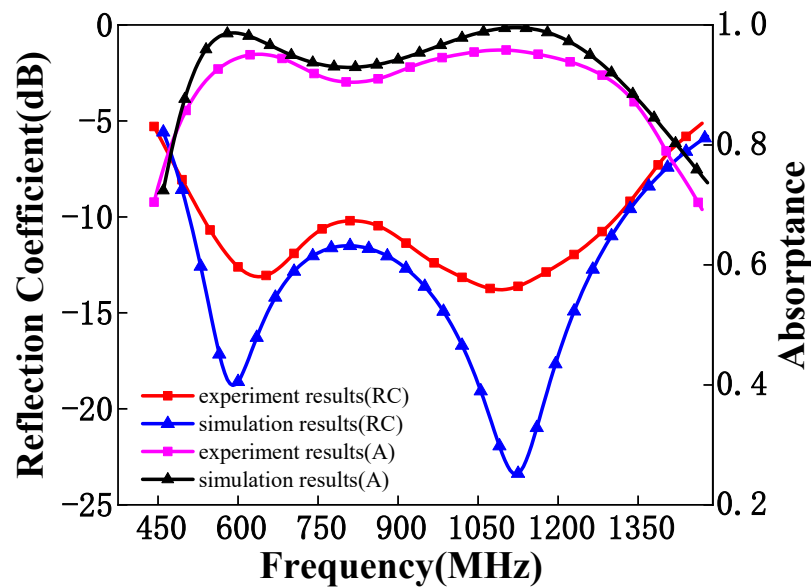


Figure 10. Comparison of reflection coefficients between simulation results and experiment results.

5. Conclusions

In this paper, a miniaturized structure of a low-frequency broadband MA was proposed. The structure connects the upper and lower surface circuits of the double-layer dielectric layer through metal holes. The size of the unit cell is $23.8 \times 23.8 \text{ mm}^2$, realizing the miniaturization of the MA. The absorption band of the MA is from 0.50 GHz to 1.33 GHz, and the unit cell forms two absorption peaks at F_L and F_H and the corresponding absorbance is 98.9% and 99.5%, respectively. With the help of the simplified equivalent circuit model, the study further analyzed the generation of double absorption peaks and physically validated the sample by the free space method. Table 1 compares the performance of the MA with other related research results. It can be seen that although the structure proposed in reference [9] achieves a larger absorption bandwidth, our work achieves absorption at a lower frequency band and successfully reduces the low-frequency response by 300 MHz, which is extremely challenging in the UHF band. Therefore, the proposed MA combines the advantages of low-frequency, miniaturization and broadband. It is expected to be widely used in the field of UHF stealth technology.

Table 1. Comparison of the proposed MA with few published MAs.

Ref.	MA Unit Structure			MA Unit Performance			
	Design Dimension	Lumped Element	Bending Wires	Absorption Band	Relative Bandwidth	Unit Size	Profile Height
[5]	2.5D	Yes (C)	No	102 MHz	/	$0.012 \lambda_L \times 0.012 \lambda_L$	$0.001 \lambda_L$
[7]	2D	Yes (L)	No	2400 MHz	/	$0.027 \lambda_L \times 0.027 \lambda_L$	$0.043 \lambda_L$
[8]	2D	No	Yes	377 MHz	/	$0.056 \lambda_L \times 0.045 \lambda_L$	$0.014 \lambda_L$
[9]	2D	No	Yes	395 MHz	/	$0.014 \lambda_L \times 0.014 \lambda_L$	$0.011 \lambda_L$
[10]	2D	Yes (R)	Yes	840–990 MHz	16.3%	$0.056 \lambda_L \times 0.056 \lambda_L$	$0.060 \lambda_L$
[11]	2D	Yes (R)	Yes	800–2700 MHz	108.5%	$0.053 \lambda_L \times 0.053 \lambda_L$	$0.071 \lambda_L$
[18]	2D	Yes (R)	Yes	1350–3500 MHz	88.7%	$0.090 \lambda_L \times 0.090 \lambda_L$	$0.097 \lambda_L$
[19]	2.5D	Yes (R)	No	1100–2000 MHz	58.1%	$0.257 \lambda_L \times 0.257 \lambda_L$	$0.088 \lambda_L$
our work	2.5D	Yes (R)	Yes	500–1330 MHz	90.7%	$0.040 \lambda_L \times 0.040 \lambda_L$	$0.075 \lambda_L$

λ_L is the wavelength corresponding to the lowest frequency. C stands for capacitor, L stands for inductor and R stands for resistor.

Author Contributions: Conceptualization, W.R., Z.X. and W.L.; methodology, P.W.; software, P.W.; validation, P.W.; formal analysis, W.R., Z.X., W.L. and P.W.; investigation, W.R. and Z.X.; resources, W.L.; data curation, W.L.; writing—original draft preparation, P.W.; writing—review and editing, P.W. and W.R.; visualization, P.W. and W.R.; supervision, W.R.; project administration, W.R. All authors have read and agreed to the published version of the manuscript.

Funding: This research received no external funding.

Data Availability Statement: The data used in this study are available on request from the corresponding author. The data can be easily reproduced from the theoretical analysis described in this study.

Conflicts of Interest: The authors declare no conflict of interest.

References

1. Landy, N.I.; Sajuyigbe, S.; Mock, J.J.; Smith, D.R.; Padilla, W.J. Perfect metamaterial absorber. *Phys. Rev. Lett.* **2008**, *100*, 207402. [[CrossRef](#)] [[PubMed](#)]
2. Yoo, M.; Kim, H.K.; Lim, S. Angular- and Polarization-Insensitive Metamaterial Absorber Using Subwavelength Unit Cell in Multilayer Technology. *IEEE Antennas Wirel. Propag. Lett.* **2016**, *15*, 414–417. [[CrossRef](#)]
3. Wu, T.; Ma, Y.-M.; Chen, J.; Wang, L.-L. Triple-band polarization-insensitive metamaterial absorber with low profile. *Int. J. RF Microw. Comput.-Aided Eng.* **2020**, *30*, e22314. [[CrossRef](#)]
4. Yoo, M.; Lim, S. Polarization-Independent and Ultrawideband Metamaterial Absorber Using a Hexagonal Artificial Impedance Surface and a Resistor-Capacitor Layer. *IEEE Trans. Antennas Propag.* **2014**, *62*, 2652–2658.
5. Khuyen, B.X.; Tung, B.S.; Yoo, Y.J.; Kim, Y.J.; Kim, K.W.; Chen, L.Y.; Lam, V.D.; Lee, Y. Miniaturization for ultrathin metamaterial perfect absorber in the VHF band. *Sci. Rep.* **2017**, *7*, 45151. [[CrossRef](#)] [[PubMed](#)]
6. Khuyen, B.X.; Tung, B.S.; Kim, Y.J.; Hwang, J.S.; Kim, K.W.; Rhee, J.Y.; Lam, V.D.; Kim, Y.H.; Lee, Y. Ultra-subwavelength thickness for dual/triple-band metamaterial absorber at very low frequency. *Sci. Rep.* **2018**, *8*, 11632. [[CrossRef](#)] [[PubMed](#)]
7. Jeong, H.; Nguyen, T.T.; Lim, S. Subwavelength Metamaterial Unit Cell for Low-Frequency Electromagnetic Absorber Applications. *Sci. Rep.* **2018**, *8*, 16774. [[CrossRef](#)] [[PubMed](#)]
8. Bui, S.T.; Yoo, Y.; Kim, K.W.; Vu, D.L.; Lee, Y. Small-size metamaterial perfect absorber operating at low frequency. *Adv. Nat. Sci. Nanosci. Nanotechnol.* **2014**, *5*, 045008.
9. Araneo, R.; Lovat, G.; Celozzi, S. Compact electromagnetic absorbers for frequencies below 1 GHz. *Prog. Electromagn. Res.* **2013**, *143*, 67–86. [[CrossRef](#)]
10. Zuo, W.; Yang, Y.; He, X.; Zhan, D.; Zhang, Q. A Miniaturized Metamaterial Absorber for Ultrahigh-Frequency RFID System. *IEEE Antennas Wirel. Propag. Lett.* **2016**, *16*, 329–332. [[CrossRef](#)]
11. Zuo, W.; Yang, Y.; He, X.; Mao, C.; Liu, T. An Ultra-Wideband Miniaturized Metamaterial Absorber in the Ultrahigh-frequency Range. *IEEE Antennas Wirel. Propag. Lett.* **2017**, *16*, 928–931. [[CrossRef](#)]
12. Li, W.; Wu, T.; Wang, W.; Guan, J.; Zhai, P. Integrating non-planar metamaterials with magnetic absorbing materials to yield ultra-broadband microwave hybrid absorbers. *Appl. Phys. Lett.* **2014**, *104*, 1189. [[CrossRef](#)]
13. Lim, D.; Yu, S.; Lim, S. Miniaturized Metamaterial Absorber Using Three-Dimensional Printed Stair-Like Jerusalem Cross. *IEEE Access* **2018**, *6*, 43654–43659. [[CrossRef](#)]
14. Yu, Y.M.; Chiu, C.N.; Chiou, Y.P.; Wu, T.L. A Novel 2.5-Dimensional Ultraminiaturized-Element Frequency Selective Surface. *IEEE Trans. Antennas Propag.* **2014**, *62*, 3657–3663. [[CrossRef](#)]
15. Shi, Y.; Tang, W.; Zhuang, W.; Wang, C. Miniaturised frequency selective surface based on 2.5-dimensional closed loop. *Electron. Lett.* **2014**, *50*, 1656–1658. [[CrossRef](#)]
16. Yu, Y.M.; Chiu, C.N.; Chiou, Y.P.; Wu, T.L. An Effective Via-Based Frequency Adjustment and Minimization Methodology for Single-Layered Frequency-Selective Surfaces. *IEEE Trans. Antennas Propag.* **2015**, *63*, 1641–1649. [[CrossRef](#)]
17. Hussain, T.; Cao, Q.; Kayani, J.K.; Majid, I. Miniaturization of Frequency Selective Surfaces Using 2.5-D Knitted Structures: Design and Synthesis. *IEEE Trans. Antennas Propag.* **2017**, *65*, 2405–2412. [[CrossRef](#)]
18. Banadaki, M.D.; Heidari, A.A.; Nakhkash, M. A Metamaterial Absorber with a New Compact Unit Cell. *IEEE Antennas Wirel. Propag. Lett.* **2017**, *17*, 205–208. [[CrossRef](#)]
19. Li, Q.; Dong, J.; Li, T.; Cao, X. Broadband Fractal Tree Metamaterial Absorber for P and L Bands Applications. In Proceedings of the 2020 IEEE 3rd International Conference on Electronic Information and Communication Technology (ICEICT), Shenzhen, China, 13–15 November 2020.